# CHANDRA
## X-ray Center   60 Garden St., Cambridge Massachusetts 02138 USA

# The HRMA User's Guide

## T.J. Gaetz and Diab Jerius

January 28, 2005, v1.42

**Abstract**

In this memo, we describe characteristics of the Chandra High Resolution Mirror Assembly (HRMA), particularly those which may affect the interpretation of the imaging data. The detailed SAOsac raytrace model reproduces many of these, at least qualitatively; however some features are not treated adequately by the current raytrace model. For example, the wings of the PSF resulting from mirror scattering are known to be seriously under predicted in the raytrace model. The known limitations of the raytrace model are described elsewhere.

## Contents

# 1   The HRMA

The *Chandra* High Resolution Mirror Assembly (HRMA) consists of a set of 4 concentric Wolter Type-I X-ray optics, their supporting structures, and a number of X-ray and thermal baffles. A schematic diagram of the optical path through the HRMA is shown in Fig. 1.
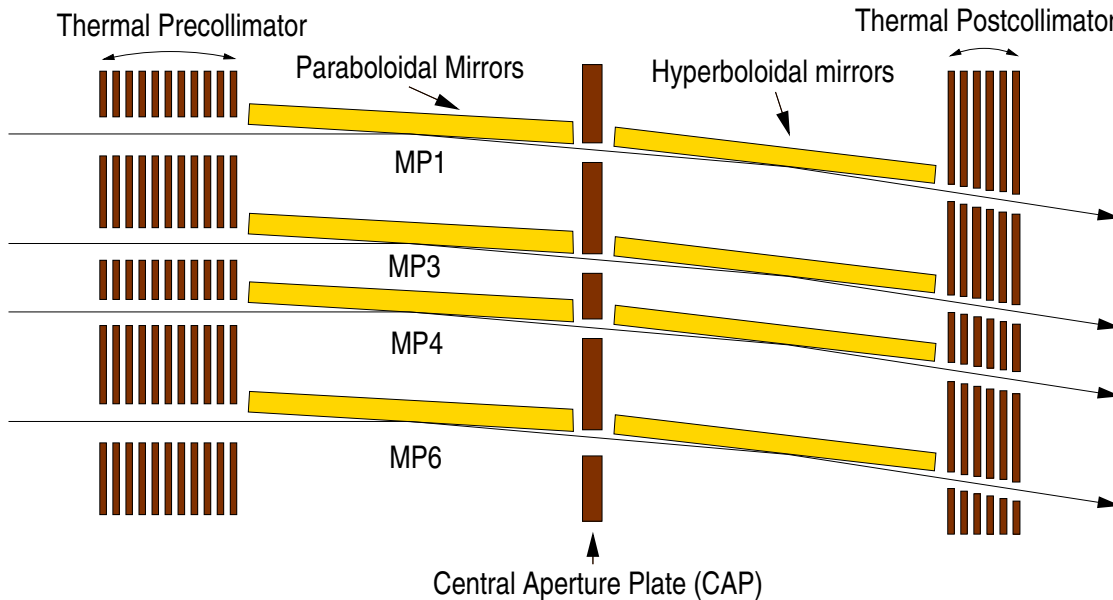


Figure 1: Schematic diagram of the optical path through the HRMA (not to scale). The focal plane is to the right. Not all structures are shown.

## 1.1   The physical layout

Each optic (mirror pair, or shell) has a paraboloidal primary mirror (P) and a hyperboloidal secondary mirror (H). X-rays focused by the HRMA reflect first from a paraboloidal mirror, then from a hyperboloidal mirror. The largest mirror pair has a diameter of $\sim$ 1.2 m, the smallest $\sim$ 0.6 m. For historical reasons, the mirror pairs are labeled, from largest to smallest, MP1, MP3, MP4, and MP6. In effect, the HRMA consists of four coaligned telescopes, with f-ratios ranging from $\sim$ 8.2 to $\sim$ 15.7. Table 1 summarizes the mirror characteristics.

Table 1: HRMA Properties

| | |
|---|---|
| focal length: | $10.07 \pm 0.003$ m |
| plate scale: | $48.82 \pm 0.02\ \mu\mathrm{m\,arcsec^{-1}}$ |
| mirror coating: | Iridium (330Å) |
| mirror diameters (1, 3, 4, 6): | 1.23 m, 0.99 m, 0.87 m, 0.65 m |
| f-ratios (1, 3, 4, 6): | 8.4, 10.4, 11.8, 15.7 |

X-ray and thermal baffles are found throughout the HRMA. They include:

- annular thermal and X-ray baffles in front of the mirrors
- X-ray baffle edges at the Central Aperture Plate (CAP) between the P and H optics
- an X-ray ghost suppression baffle for the paraboloidal element of MP6

- annular thermal baffles between the mirrors and the focal plane (in front of the transmission gratings)
- radial support struts, including the aspect system periscope (shadowed by a CAP strut)

The annular baffles include a set of 12 radial struts spaced at 30° intervals. For on-axis sources, the support struts in the CAP shadow the other support struts.

## 1.2 General Optical properties

The focal surfaces of the mirror pairs are approximately quadratic, curving toward the HRMA with increasing source off-axis position. Each mirror pair has a different focal surface, with that of the smallest mirror pair (MP6) having the strongest curvature and that of the largest (MP1) having the weakest curvature. Fig. 2(a) illustrates this behavior.
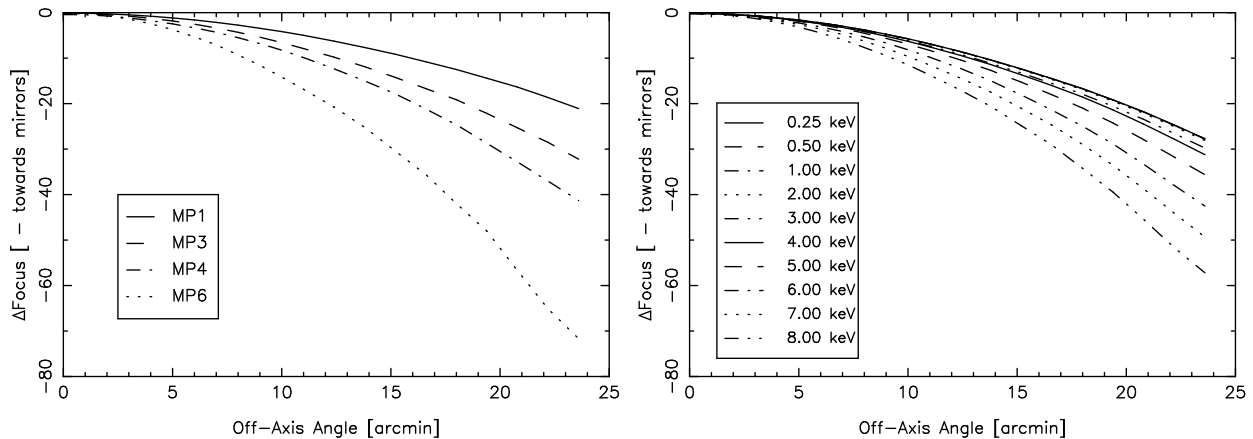
(a) Mirror pair focal planes          (b) Energy dependence of the HRMA focal plane

Figure 2: Mirror pair and HRMA focal planes

X-ray reflectivity is a strong function of the incident energy. Fig. 3(a) shows the total HRMA and mirror pair effective areas as functions of energy. The rapid drop in effective area just above 2 keV is caused by an absorption edge in Ir, the reflective material used to coat the optics. X-ray reflectivity is also a strong function of the incident graze angle. Due to the nested nature of the HRMA mirrors, each pair has a different mean grazing angle, ranging from $50.6'$ for MP1 to $26.7'$ for MP6. For a given energy, the reflectivity rapidly drops for graze angles exceeding a critical graze angle, and conversely, for a given graze angle, the reflectivity drops rapidly for energies exceeding a corresponding critical energy. At low energies, all of the mirror pairs reflect on-axis photons relatively efficiently. As energy increases, the nominal graze angle becomes larger than the critical graze angle for the larger mirror pairs; this produces the decline in mirror pair effective area with increasing energy. Each mirror pair is in effect "tuned" to have a different high-energy cutoff, and its fractional contribution to the total effective area is energy dependent. Fig. 3(b) shows the fractional contribution of each mirror pair to the HRMA effective area as a function of energy. Because of the loss of effective area from the larger mirror pairs as energy increases, higher energy photons will be best focused on the MP6 focal plane, while lower energy ones are best focused on a

(a) HRMA effective area and individual shell effective areas

(b) Fractional contribution of the four mirror pairs to the overall HRMA effective area.
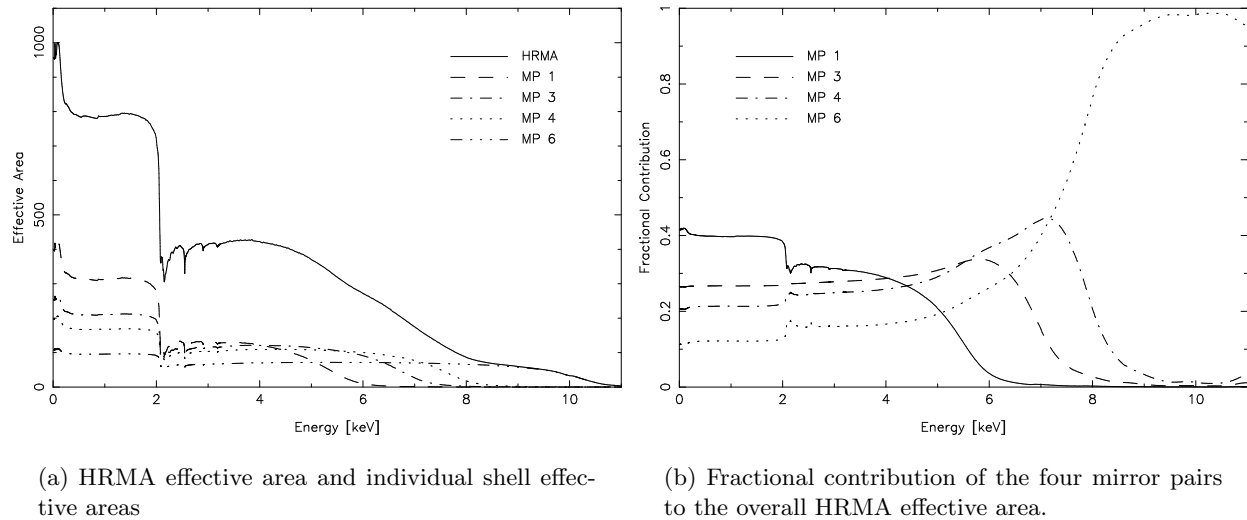
Figure 3: Effective Area

geometrically-weighted focal plane. This difference manifests itself as an overall energy dependence in the best-focus HRMA focal plane, which is illustrated in Fig. 2(b).

The divergent focal planes preclude a perfectly focused image, except on-axis. Since no source is monochromatic, there is no single off-axis focal surface which is appropriate. The detectors do not (and can not, physically) follow the focal surfaces for the individual HRMA mirror pairs. The ACIS-I chips are tilted to approximately follow a mean HRMA focal surface. The ACIS-S chips and HRC-S plates are tilted to approximately follow a Rowland circle (to form the correct focal surface for the transmission gratings), which has less curvature than the mean HRMA focal surface. The HRC-I is flat, and does not follow the curvature of the focal surface away from the optical axis.

The image shape and size vary strongly as a function of the spectral distribution of the source in addition to the off-axis angle. Fig. 4 illustrates the extreme in the variation in focus with energy for far off-axis HRC-I imaging.

## 1.3   Known Imperfections

The HRMA, while wonderful, is not perfect. One can classify its deviations from ideal as:

- Figure errors (PSF core)
  The mirror figures deviate from the ideal shapes. Low spatial-frequency errors in the figures exist due to errors in polishing and figuring and stresses induced by the mirror supports. The HRMA suffers from minor figure errors, predominantly axial, which do not produce asymmetries in the on-axis PSF. The struts are aligned azimuthally with the areas where the mirrors are glued to their support structure, and thus tend to mask surface deviations caused by the interface. The figure errors are worst in the largest mirror pair (MP1).

- Surface roughness (scattering; PSF wings)
  These are high spatial-frequency errors in the smoothness of the surface. The roughness of the mirror pairs vary, with MP1 being the worst and MP6 the best. Rougher surfaces tend to scatter higher energy photons more than lower energy ones, thus "puffing out" the PSF at higher

Ideal Focal Plane

0.25 keV          0.5 keV          1.0 keV          2.0 keV          3.0 keV

0.25 keV          0.5 keV          1.0 keV          2.0 keV          3.0 keV

HRC-I

Ideal Focal Plane

4.0 keV          5.0 keV          6.0 keV          7.0 keV          8.0 keV

4.0 keV          5.0 keV          6.0 keV          7.0 keV          8.0 keV
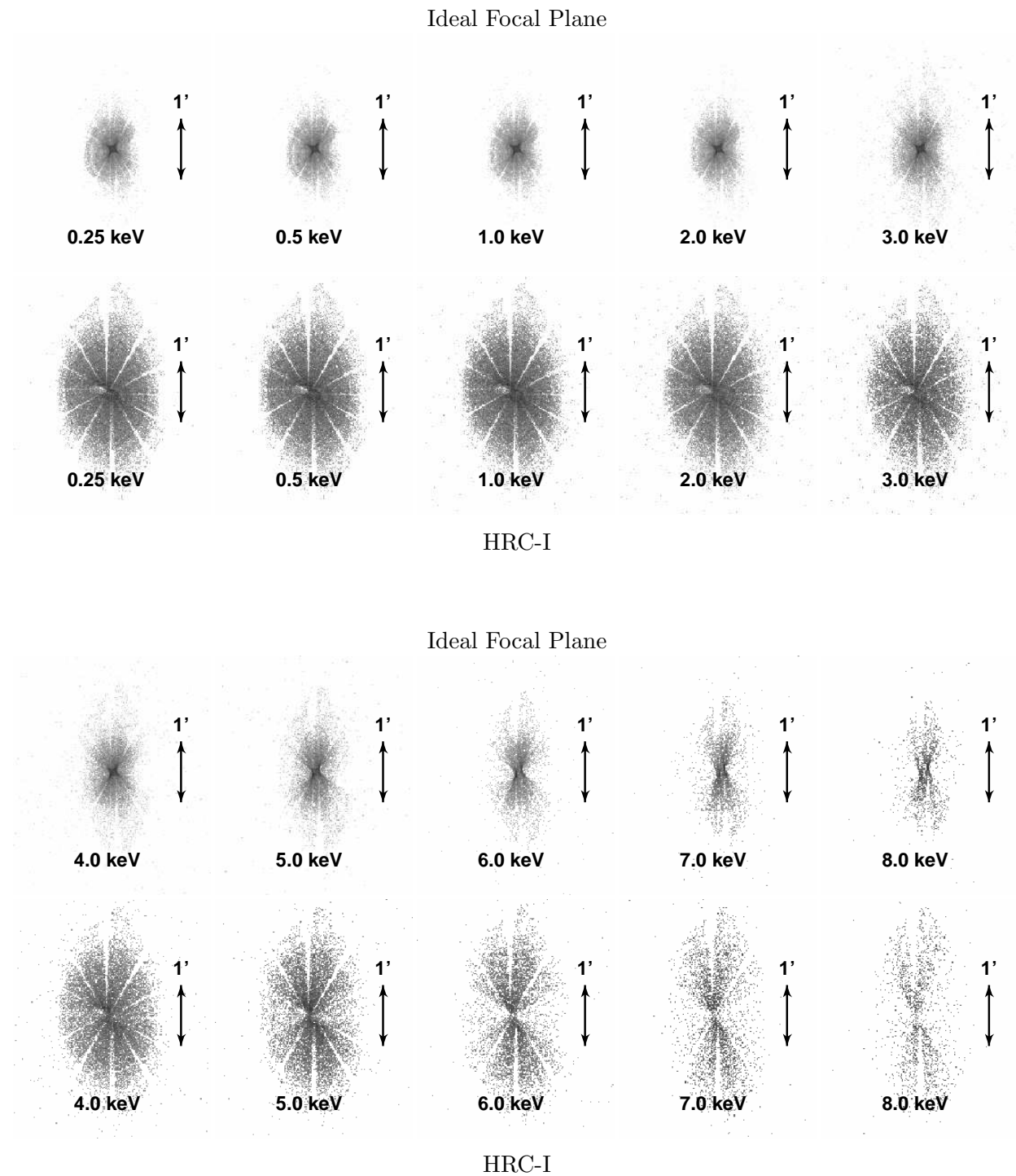
HRC-I

Figure 4: Effect of divergent focal plane on image quality as a function of energy for a 23.6′ off-axis source (logarithmic stretch). The upper panels show the PSF for an ideal mean HRMA focal plane, while the lower panels show the PSF on the actual HRC-I focal plane.

energies. Because of the grazing incidence geometry, the scattering is predominantly "in-plane" (*i.e.*, radial). See §5 for further details.

- Alignment errors (PSF, on-axis and off-axis)
  These are errors in the positioning of the optics, between the mirrors in each pair, as well as between the mirror pairs. Each mirror pair has a systematic lateral (i.e. perpendicular to the axes of revolution) misalignment (also known as a *decenter*) between its mirrors, with approximately the same magnitude and direction. Additional systematic tilts between the mirrors in each pair compensate for the offset, resulting in negligible on-axis coma but producing significant off-axis aberrations. MP6 also has a significant residual P to H tilt producing some on-axis coma ($\sim 0.32''$ radius). The on-axis foci of the mirror pairs span an axial range of $\sim$0.45 mm, with the foci of the smaller mirror pairs straddling the system focus. This produces a slight shift with energy in the mean HRMA focus, and PSF blur of $\sim$0.2''-0.4'' diameter at very high energies (where the effective area is small).

- Energy- and Grazing Angle-dependence of reflectivity (off-axis PSF)
  The reflectivity depends on the angle at which the X-ray is incident on the surface. For off-axis sources, the incident graze angle varies around the optic, so that parts of the PSF are selectively enhanced or suppressed. The angle-dependence is greatest at high energies; this effect can be seen in Fig. 4 where the PSF becomes fainter along the shorter axis as the energy increases, and becomes increasingly bow-tie shaped.

- Obstructions in the optical path (shadows)
  The radial support struts produce shadows in the PSF; mirror scattering does not fill in the shadows because mirror scattering is predominantly radial. Annular baffle edges also introduce vignetting for angles exceeding $\sim 14'$ off-axis.

- Vignetting
  Because of the finite lengths of the mirrors, the X-rays are vignetted for off-axis sources. The vignetting is strongly energy dependent at higher energies. Beyond $\sim 14'$ off-axis, the annular X-ray baffle edges introduce additional vignetting. In addition to the reducing the effective area, vignetting affects the PSF shape at far off-axis angles (contributing to the "bow-tie" effect).

## 1.4   Interaction with Detectors

The ability to utilize the full HRMA resolution is dependent upon the quirks of the detector used to image the focused photons. The ACIS detectors have a pixel size of $\sim 0.5''$, while the HRC detectors have an approximately Gaussian resolution function with a FWHM of 18 $\mu$m ($\sim 0.37''$). The HRC also shows systematic artifacts in the determination of event positions, which adds an additional $0.3'' - 0.5''$ blur if left uncorrected (Juda, 2002; Jerius, 2002). Incomplete aspect reconstruction also results in a residual image blur; this is of import only for on-axis images (see Aldcroft (2002) for more information).

# 2   Anatomy of the on-axis PSF

For most applications, the on-axis PSF is well represented by a radially symmetric distribution. (Detailed structure in the PSF is not resolvable due to the detector artifacts mentioned in §1.4). Figs. 5 and 6 represent the PSF as the fraction of the total energy enclosed within a circular
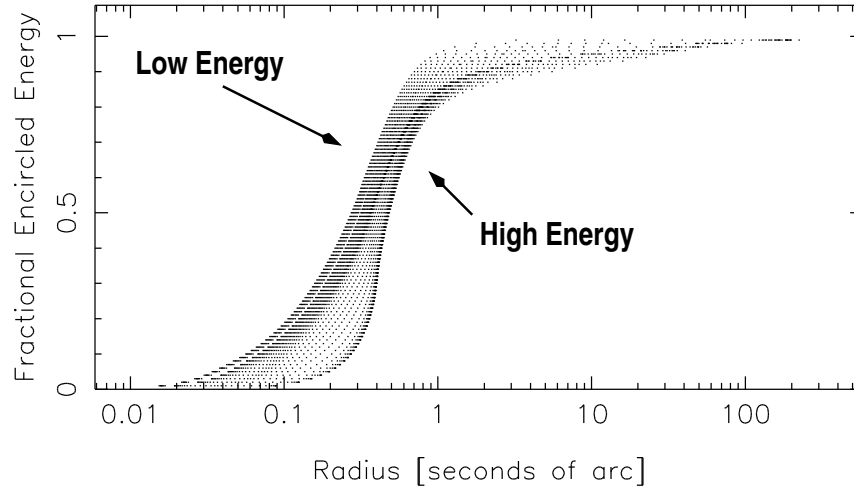
Figure 5: On-axis encircled energy fractions for $E = 0.25$ keV to 10 keV (from simulations).
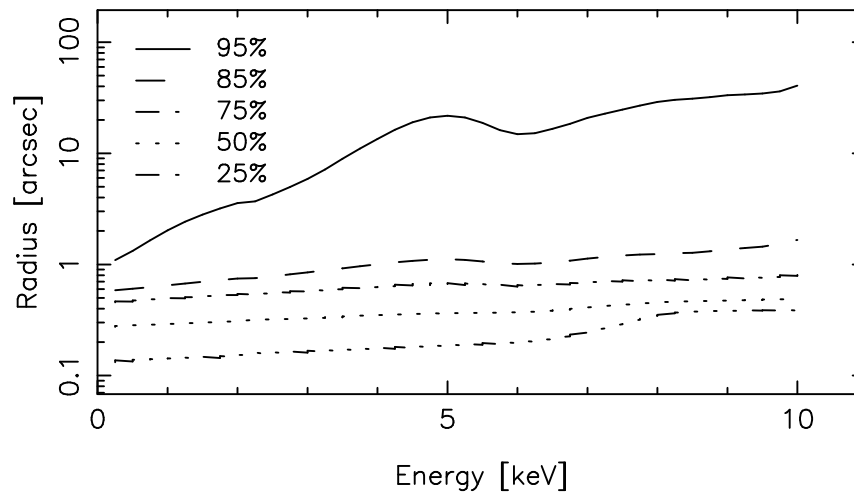


Figure 6: Dependence with energy of the radii for interesting encircled energy fractions (from simulations).

aperture. The PSF broadens dramatically at higher energies. Note that the simulations shown in Figs. 5 and 6 underestimate the flux in the PSF wings; see §5 for a more detailed discussion.

The MP6 P to H residual tilt (§1.3) produces on-axis coma (a circular ring-shaped artifact) of $\sim 0.6''$ diameter in on-axis images; the center of the nonuniform ring is somewhat offset from the image core. This "tilt ring" generates the appearance of an extended source of $\sim 0.6''$ diameter. Because MP6 provides most of the effective area at higher energies (see Fig. 3), the effect is most noticeable for harder sources, but is present at all energies. Fig. 7 shows the PSF variation with energy; the distortions at higher energies are due to the MP6 tilt.

# 3 Anatomy of the off-axis PSF

As mentioned in §1.2, the combination of divergent focal planes and detector surfaces produce distortions in the off-axis image, in addition to the aberrations intrinsic to the Wolter Type-I geome-
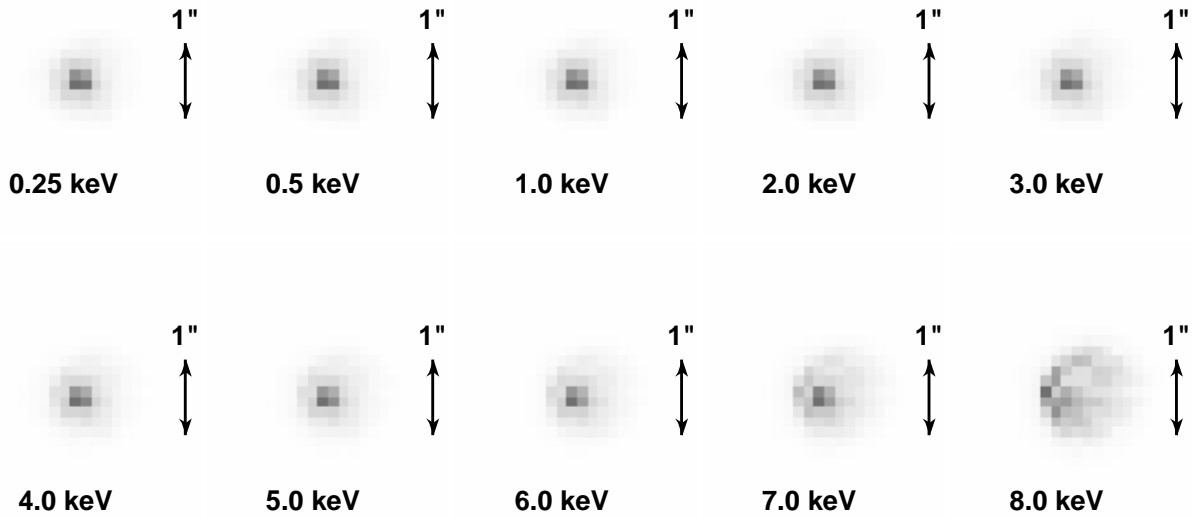
Figure 7: Change in the on-axis PSF with energy, at HRC-I resolution (from simulations).

try. The mirror misalignments mentioned in §1.3 produce significant additional off-axis aberrations varying as $\sim\phi/2$.

The dominant off-axis aberration of the Wolter Type-I geometry is a radial squashing and tangential stretching of the image to form an "eye"-like image. For ideal optics, the orientation of this aberration varies directly with angle, $\phi$; the long axis of the "eye" is tangent to a circle centered on the optical axis. The size of the PSF scales roughly (but more slowly than) quadratically with off-axis angle, $\theta$ (Fig. 8).

By themselves, the decenter misalignments of the P and H mirrors (§1.3) would introduce circular artifacts ("coma") into the on-axis image, similar to the residual coma ("tilt ring") in MP6 (§2). However, the assembly process introduced a compensating tilt between the mirrors in each pair, so that the coma from the relative tilt mostly cancels the coma from the decenter. Consequently, we term this combination of decenter and tilt a "coma-free decenter misalignment" of the optics. The coma-free decenter induces additional off-axis aberrations. Some of the features of the off-axis PSF are illustrated in Fig. 9. For an off-axis image at best focus, the core of the image is folded to form overlapping bright cuspy diamond-shaped features. In practice, the off-axis PSF is somewhat out of focus; this causes the diamond-shaped features to partially unravel, forming a bright oval feature; this is evident in Fig. 4 which compares imaging on the ideal focal plane to that on the actual HRC-I focal plane.

The bright features in the core are caustics; the oval feature and especially the points of the cusps can have high surface brightnesses. For very bright sources, this can result in ACIS pileup, even for sources far off-axis. These additional aberrations vary as $\phi/2$; this $\phi$-dependence is most noticeable in the orientation of the cuspy box in the center of the image (and the orientation of the bright oblong oval feature when the image is somewhat out of focus).

When the images are sufficiently out of focus, as for ACIS-S or the HRC detectors far off-axis, the cuspy feature completely unravels to produce a hole in the center of the image. ACIS-I observations
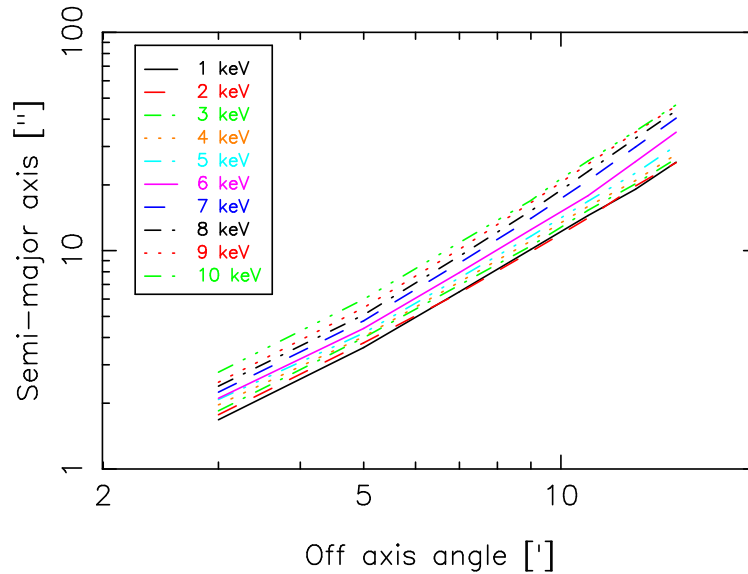
Figure 8: Dependence with energy of the 85% Enclosed Count Fraction (ECF) semimajor axis (from simulations). The PSF size scales with off-axis angle $\theta$ somewhat more slowly than quadratically. At fixed off-axis angle, the PSF size increases with energy.

tend to be intermediate, with a bright oblong core oval containing cuspy corners.

In images with sufficient signal to noise, a bulge in the outer rim of the image can also be seen to vary as $\phi/2$, so that for a given off-axis angle $\theta$, the image is stretched to a greater or lesser degree, depending on the value of $\phi$. This can be readily seen in Fig. 10, which shows simulations of point sources at 5′ and 10′ off axis; note particularly $\phi = 60°$ *vs.* $\phi = 240°$. Note that the bulge in the outer envelope tends to be aligned with the bright oval structure in the center of the image.

The support struts cast shadows. Opposing strut shadows are roughly parallel, but do not necessarily line up on opposite sides of the image; this is another consequence of the broken symmetry of the system.

With sufficiently high resolution (and sufficiently good spatial sampling of the PSF), wavy, approximately tangential features appear, labeled "ripples" in Fig. 9. These are the result of low frequency axial waves in the figures of the optics. The ripple features are caustics, analogous to the patterns seen at the bottom of a swimming pool: X-rays are selectively focused and defocused to produce bright narrow features with darker spaces between. Low-frequency azimuthal figure errors also exist: They produce higher frequency image distortions and are not as obvious in off-axis images; the detector resolution is not good enough to see them in on-axis images.

As shown in Fig. 3, the contribution of each shell to the total effective area varies with energy. Consequently the detailed off-axis PSF depends on the spectrum of the source, the detector used, and source's radial and azimuthal position (because of the coma-free decenter aberrations discussed above).

Detect algorithms may be sensitive to different features of the off-axis PSF. The ellipse parameters produced by the CIAO tool `celldetect` are sensitive to the orientation of the bright oblong core feature: for sufficiently bright sources, the angle of the ellipse correlates with $\phi/2$. (Note that the phase of this effect is relative to a frame fixed with respect to the telescope [MSC coordinates]; in "sky" data, the roll of the telescope needs to be accounted for.)
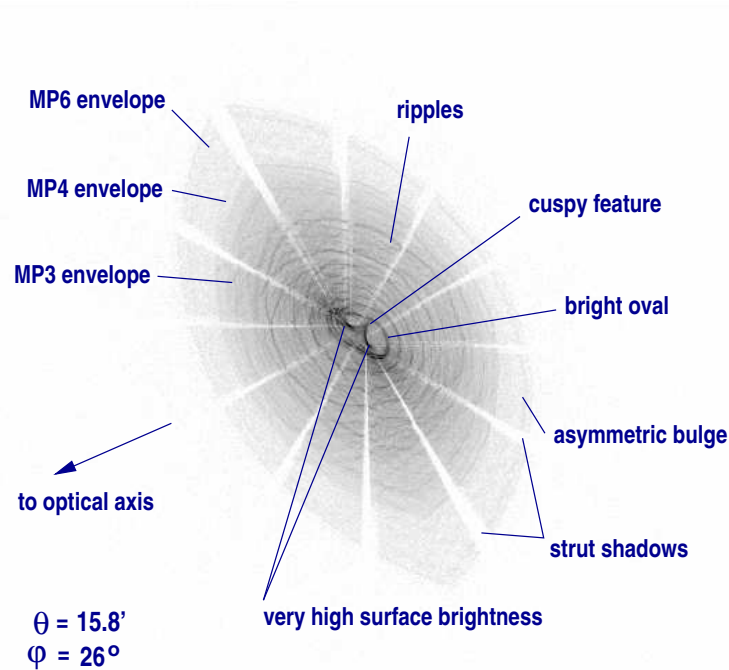
Figure 9: A high-resolution simulation of a point source 15.8′ off-axis, indicating features of interest. Note that the indicated structure is entirely from direct image, the *core* of the PSF (that is, quasi-specular reflections from the optics). The mirror scattering wings are much fainter than the off-axis direct image.

The above discussion of off-axis image refers entirely to the direct image, the "core" of the PSF, resulting from quasi-specular reflection from the optics. The mirror scattering is much fainter than the direct image, and little is currently known about the effects of mirror scattering on the far-off-axis PSF.

# 4   Bright PSF substructure

The detector surfaces do not follow the individual mirror pair focal surfaces; for off-axis images, the images resulting from the individual mirror pairs are to some degree slightly out of focus. This defocus causes the cuspy core feature resulting from the coma-free decenter misalignment to partially unravel. Typically, part of the diamond caustic structure unfolds to form a bright elongated oval structure surrounding the rest of the cuspy core structure. These structures are all caustics: They can have very high surface brightness, particularly the corners of the diamonds; see for example, Fig. 9. Because of the high surface brightness of the cusp corners and Poisson fluctuations, single point sources can appear to be lumpy, or have multiple close components, particularly if the number of counts is small and the PSF is not well sampled. For example, Fig. 11 displays a simulation of a point source which produces two bright spots.
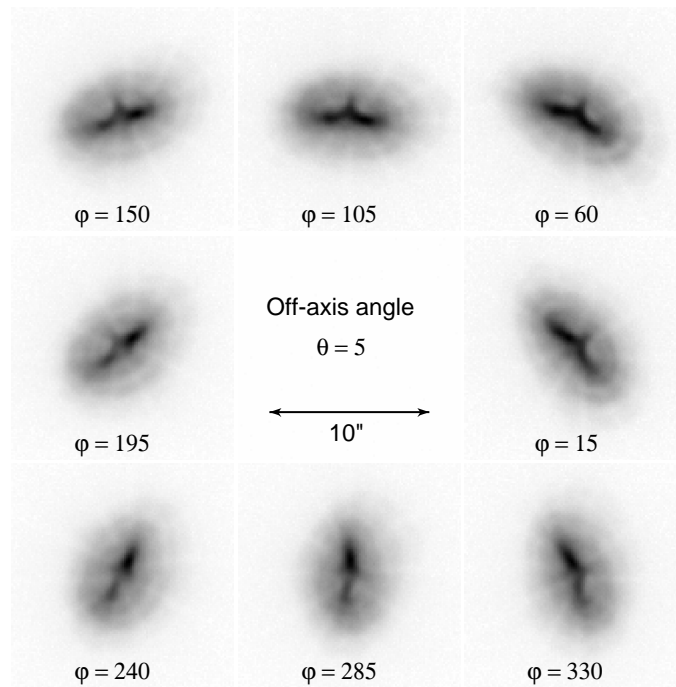
(a) $\theta = 5'$ off-axis, $0.125''$ binning; $10''$ scale bar
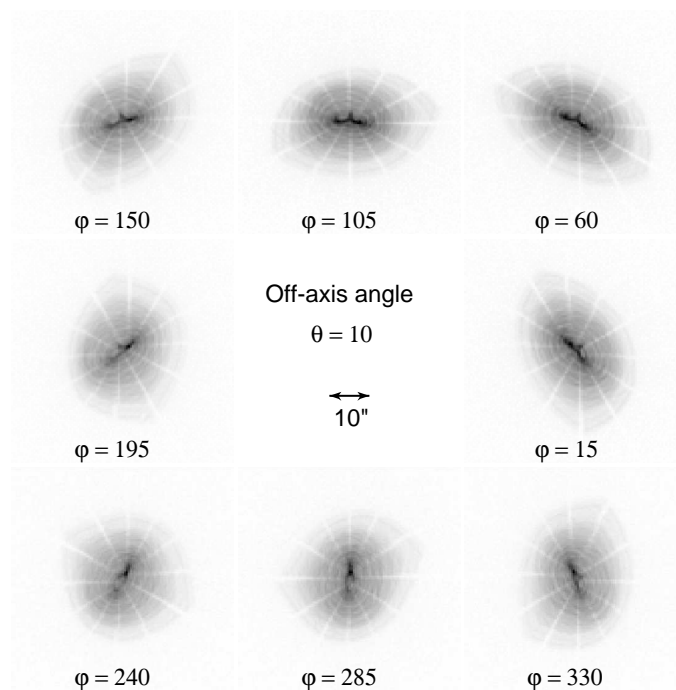


(b) $\theta = 10'$ off-axis, $0.5''$ binning; $10''$ scale bar

Figure 10: Simulations of well-sampled monochromatic point sources (1.5 keV) for $\theta = 5'$ and $\theta = 10'$ off-axis. The simulations are spaced at intervals of $45°$ in $\phi$, starting at $\phi = 15°$. These are projected to the HRC-I focal plane.
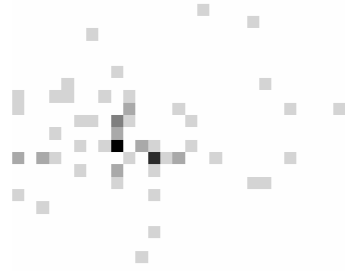
Figure 11: Simulation of a point source 6.9′ off-axis (66 counts). The combination of high surface brightness at the points of the cuspy feature and Poisson fluctuations produces two bright pixels separated by $\sim 2''$. Superficially this might appear to be a pair of sources, but it is a single source.

## 4.1   Analysis Issues

- The off-axis PSF varies systematically with off-axis angle, $\theta$, and azimuth, $\phi$. This results in a stretching of the PSF. Note that the direction of the stretch varies roughly as $\phi/2$ rather than directly as $\phi$. This stretching could be mistaken for source extent.

- The off-axis image aberrations can mimic multiple sources, particularly if the source is not very bright and the structure of the PSF is not well sampled. The coma-free decenter aberration produces bright cuspy features in the image of a point source. Because the surface brightness tends to be highest in the cuspy corners, in faint sources the corners may stand out against the fainter surrounding source image giving the impression of a pair or triplet of sources. This can also fool detection algorithms; Kim et al. (2004) note a case of a point source with $\sim 2000$ counts being detected as two closely-spaced sources because of these aberrations.

  Suspected double or triple sources with separation smaller than the characteristic PSF size for the given off-axis position should be compared with SAOsac (ChaRT) simulations with the same spectrum and off-axis angle as the source, and with a similar number of counts as the observed source. If the separations and position angles of the observed sources are comparable to those for the cusps in the simulation, the multiple sources may be artifacts of the image aberrations. The distribution of X-rays is a random process: a number of instantiations should be generated using different seeds, in order to guard against accidentally obtaining pathological cases, and to assess the effects of Poisson clumping.

## 5   Mirror scattering halo

The HRMA PSF has a faint halo extending to large angles. The mirror scattering is energy dependent and the scattered spectrum gets harder with increasing angle from the source.

This is the result of X-rays scattering from microroughness on the mirror surfaces. Current estimates are that $\sim 1.3\%$ of the power at 1.5 keV, ($\sim 7\%$ of the power at 6.4 keV) is scattered beyond $20''$.

The *Chandra* on-axis PSF can be divided approximately into two regimes (see Fig. 12):

- the core, consisting of quasi-specular X-rays reflecting from the mirror surface (including low-frequency mirror figure errors and deformations)
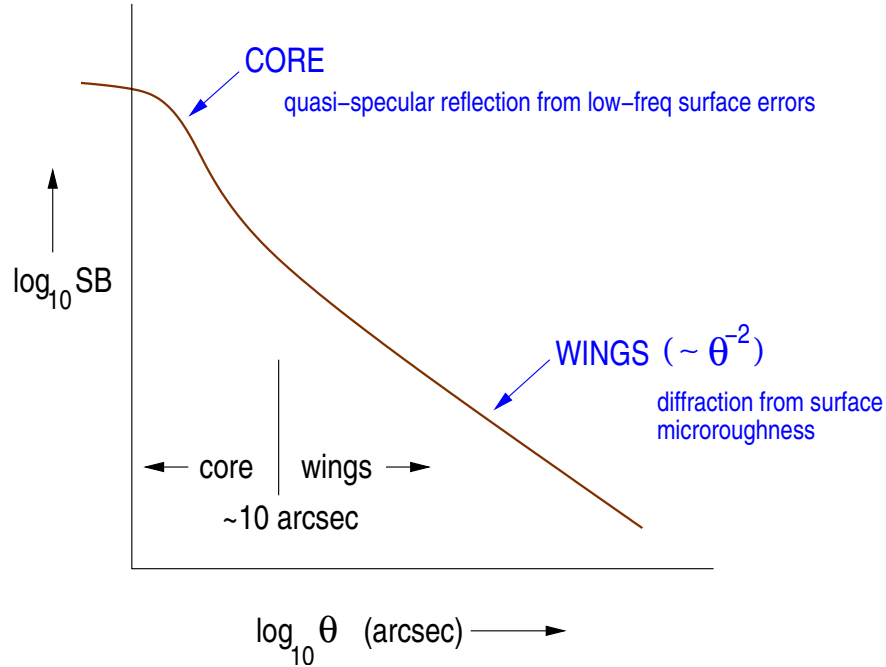
Figure 12: Schematic of the on-axis PSF as a function of angular distance from the core.

- the wings, consisting of reflected/diffracted X-rays which scatter off the high spatial frequency components of the surface. These are energy-dependent; they fall very roughly as $\theta^{-2}$, where $\theta$ is the angular distance from the core.

## 5.1  Empirical Model

An empirical model based on the ground calibration measurements has been generated. Data for individual quadrants of mirror pairs at different energies and off-axis angles were combined, and a scaling model developed to allow surface brightness profiles to be generated for different energies. A number of systematic effects remain to be accounted for; the uncertainties are probably at least 30-50%. This model is described more fully in Gaetz (2004b).

## 5.2  Calibration Observation: Her X-1

A deep calibration observation of Her X-1 (obsid 3662) was obtained in order to improve the understanding of the PSF wings. This object was chosen as a bright X-ray source (so as to see the PSF wings well above the detector background) with a small $N_H$ column (to minimize any contribution from a cosmic dust X-ray scattering halo) and relatively uncluttered background (to minimize the contribution of cosmic sources to the PSF wings estimate). Because the source is very bright, the inner parts of the wings ($\lesssim 15''$) are heavily piled up, but the brightness of the source allows the wings to be probed at large angles.

The SIM was shifted to move the optical axis to $\sim 1'$ from the edge of the S3 detector furthest from the frame store; a Y-offset moved the image $\sim 1'$ into node 0 of the detector. The resulting pointing is $\sim 45''$ off-axis. The nominal graze angle for the smallest mirror pair is $\sim 27'$, so this is effectively on-axis with regard to the mirror scattering properties. Fig. 13 is an image of the
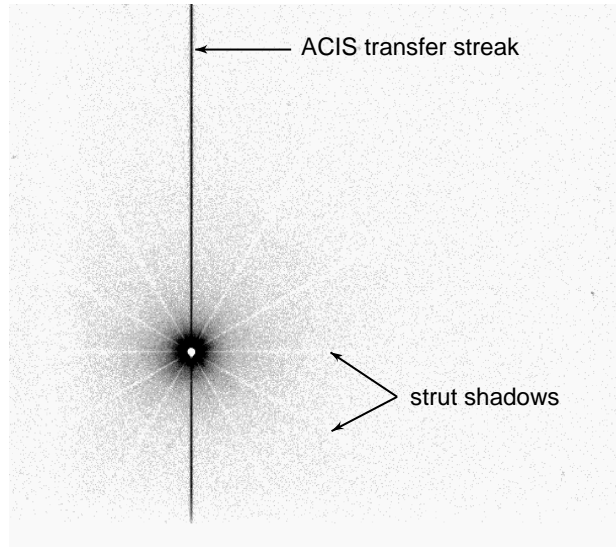
Figure 13:  The calibration observation of Her X-1 (obsid 3662), shown in the telescope reference frame.
The core of the source is bright enough to show the shadowing by the support struts. Note that
the ACIS transfer streak is aligned with strut shadows. The source is heavily piled-up, producing
the characteristic hole in the core. The image was energy-filtered (0.35-5.0 keV), binned on sky
pixels, and a logarithmic intensity stretch was applied.

Her X-1 calibration data; the mirror scattering halo is evident, and is bright enough that the strut
shadows can be seen clearly. (This indicates that the mirror scattering halo is much brighter than
any diffuse scattering halo from dust along the line of sight.) The analysis of these data is described
in Gaetz (2004a).

Radial profiles of the Her X-1 scattering wings for 1.0-2.0 keV and 3.0-4.0 keV are plotted in Fig. 14.
A powerlaw plus exponential cutoff model is overplotted; the fit applies for $\theta > 15''$. The results
for the empirical ground-based model are also plotted. The agreement is reasonably good above
$\sim$2 keV, but below 2 keV, the agreement is less satisfactory. In all cases, the ground-based empirical
model overpredicts for $\theta \lesssim 20''$; the reason for this is not presently understood. For comparison, the
*Chandra* 1.0-2.0 keV Her X-1 radial profile is also compared in Fig. 15 to the *ROSAT* PSPC PSF
profiles for 1.0, 1.5, and 2.0 keV; *ROSAT* also featured very smooth X-ray optics. The energy
dependence of the profiles is compared in Fig. 16.

The mirror scattering is in large part diffractive, and the scattering angle depends on the incident
X-ray energy; this is illustrated in Fig. 17. Spectra were extracted from annular regions centered
on Her X-1 (obsid 3662). To account approximately for the intrinsic spectrum of Her X-1, the
spectra were divided by a spectrum extracted from the ACIS transfer streak for the core of the Her
X-1 image. The steepening with annular radius of the low energy profiles is a consequence of the
spectral hardening.

## 5.3   Analysis Issues

- There remain significant uncertainties in the PSF wing profile at large angles. The diffuse
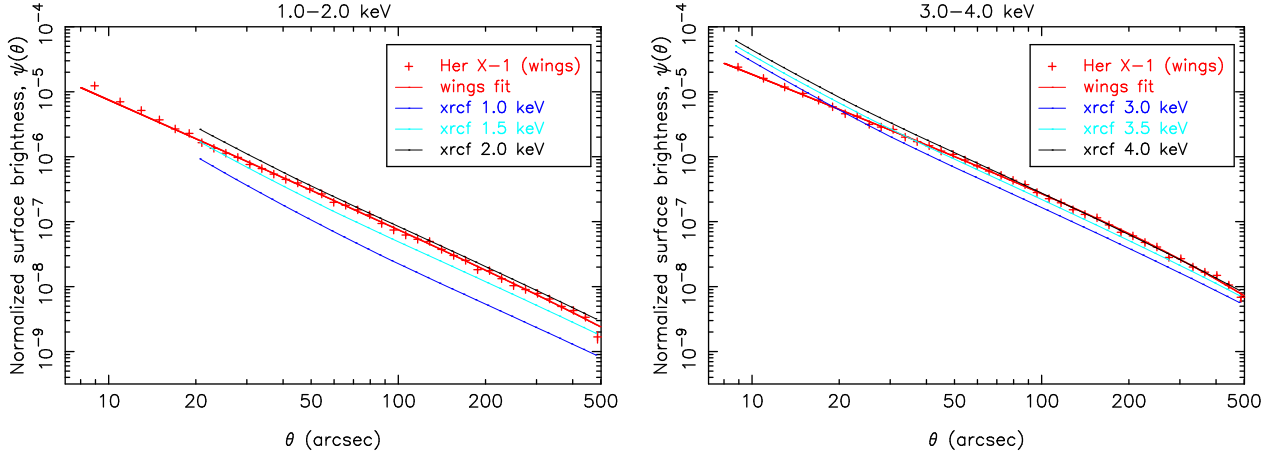  mirror scattering halo is energy dependent, with hardness increasing radially outward.

Figure 14: Radial profiles of the Her X-1 scattering wings for 1.0-2.0 keV (left panel) and 3.0-4.0 keV (right panel). The results for the empirical ground-based model are also plotted.
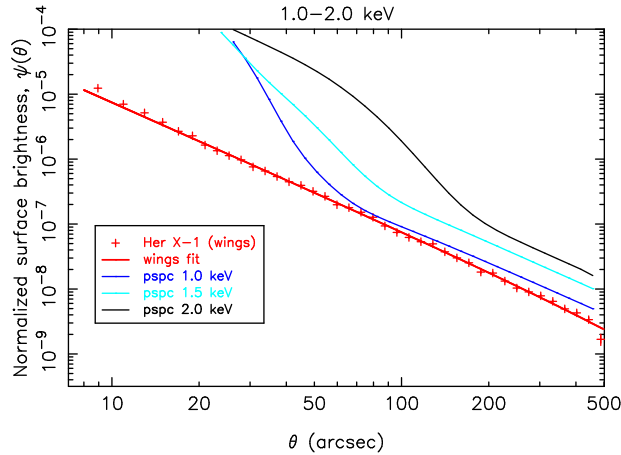


Figure 15: Radial profile of the Her X-1 scattering wings for 1.0-2.0 keV compared to the *ROSAT* PSPC wings profile. The PSPC profile was evaluated using the parameterization of Boese (2000).

## 6   Strut Shadows

The support struts in the HRMA structure produce shadows in X-ray images; these are a set of 12 dark spokes crossing the image.

These are most readily seen in sufficiently well sampled images; see Figs. 9 and 13 for example. Because of an intrinsic HRMA internal misalignment, the spokes are not aligned in off-axis images: opposing strut shadows may have lateral offsets (Fig. 9). This is a result of the coma-free decenter misalignments of the HRMA, which breaks the axial symmetry of a pure Wolter Type-I X-ray mirror. Normally, the spokes are not readily evident in on-axis images; however, they may be seen in the mirror scattering halo of extremely bright point sources (such as in the calibration observation of Her X-1 ,ObsID 3662; see Fig. 13). The strut shadows might also produce artifacts if images of bright sources are followed to very low surface brightness levels.
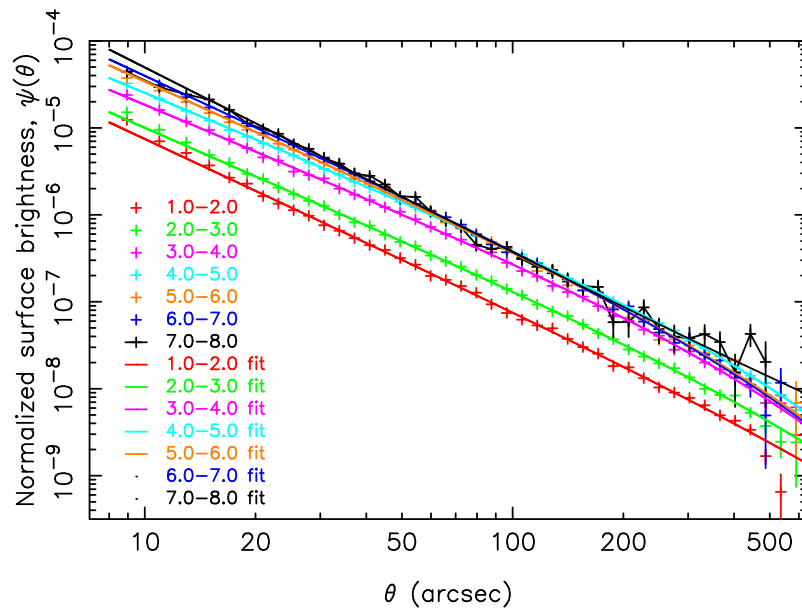
Figure 16: Comparison of the radial profiles for the diffuse mirror scattering for different energies. The profiles are fit only for $\theta > 15''$ but are plotted down to $8''$ for comparison. The legend indicates the energy band in keV. See text.
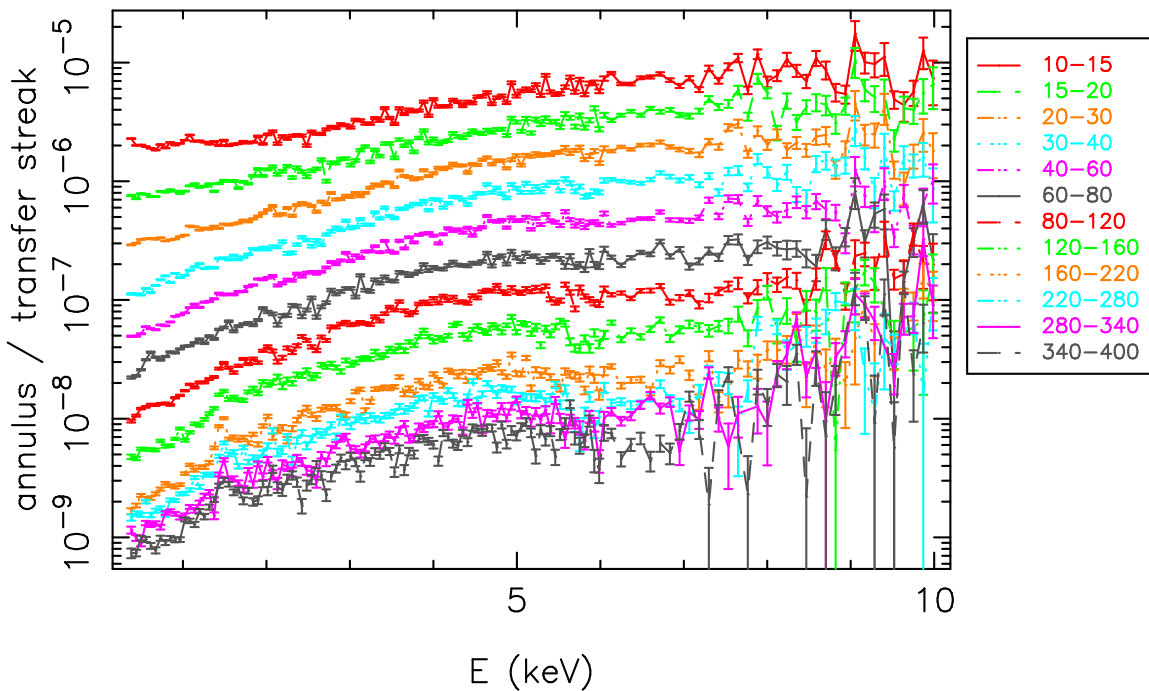


Figure 17: Comparison of spectra for the diffuse mirror scattering wing emission. The spectra extracted for the annuli are normalized by dividing by a spectrum extracted from the ACIS transfer streak. The legend indicates the annular angle range in arcsec. See text.

## 6.1   Analysis Issues

- Be aware that the HRMA support strut shadows (and mirror support dimple deformations) induce a 12-fold symmetry in the on-axis PSF. Be wary of low surface brightness features with roughly evenly spaced lobes (especially 12). Note that this symmetry is in a frame attached to the telescope; the roll of the telescope for a given observation should be taken into account by either derolling the data, or by applying the roll to the PSF, before comparing the two.

# 7   Vignetting

The energy-dependent vignetting function depends on two factors: purely geometric vignetting, and mirror surface (reflectivity and scattering) properties. Purely geometric vignetting is determined by the geometry of the optics, baffles, and obstructions in the system. The reflectivity depends on the X-ray energy and the graze angle of the X-ray incident on the optic. For an ideal system, the graze angles for on-axis X-rays will vary slightly axially along the optic. For off-axis sources, the graze angle can vary strongly azimuthally around the optic; the most favorable and least favorable graze angles are in the plane containing the optical axis and the off-axis source direction.

Off-axis, the graze-angles (and hence, reflectivity) vary markedly and systematically around the optic for off-axis sources. On the side of the optic closest to the source direction, the graze angles become shallower (increasing the reflectivity), and on the opposite side, the graze angles become steeper (decreasing the reflectivity). A photon hitting the P optic with shallow graze angle will, if it intercepts the H optic, tend to reflect from the H with a steeper graze angle, reducing the reflectivity gain from the P optic. In any case, the loss of geometric area due to geometric vignetting (eventually) overcomes any improvement in reflectivity in the plane containing the source. Near the "sides", on the other hand, the variation in graze angle with source direction is much less extreme (a cosine effect), and the increasing concentration of geometric area towards the plane perpendicular to the source direction dominates the off-axis effective area. Thus, the dominance of the "sides" of the mirrors for larger off-axis angles results from a combination of retaining favorable graze angles and retaining geometric area.

The misalignments between the optics induce an angular dependence on the vignetting; the energy and angle dependences are illustrated in Fig. 18.

# 8   Single-reflection ghosts

**Sources far off-axis can produce faint single-reflection "ghosts".**

Single-reflection ghost images occur when the photons reach the focal plane after missing either the paraboloid or the hyperboloid component of a given mirror pair. Photons which reflect off only a paraboloid component focus at approximately twice the system focal length (if not intercepted by the H optic or a baffle), while photons which reflect off only a hyperboloid component focus (poorly) at about half the system focal length (unless intercepted by a baffle). If only a P or H optic were present, then at the location of the system (P + H) focal plane, the photons would form diffuse rings with radii about half of the optic radius. As sources move off-axis, these rings deform, forming cardioid-like cusps when the off-axis angle is about the nominal graze angle for the optic, then forming portions of limaçon-like loops as the source moves further off-axis. Once the ghost has cusped and formed a loop, the direct image coincides with the intersection of the double
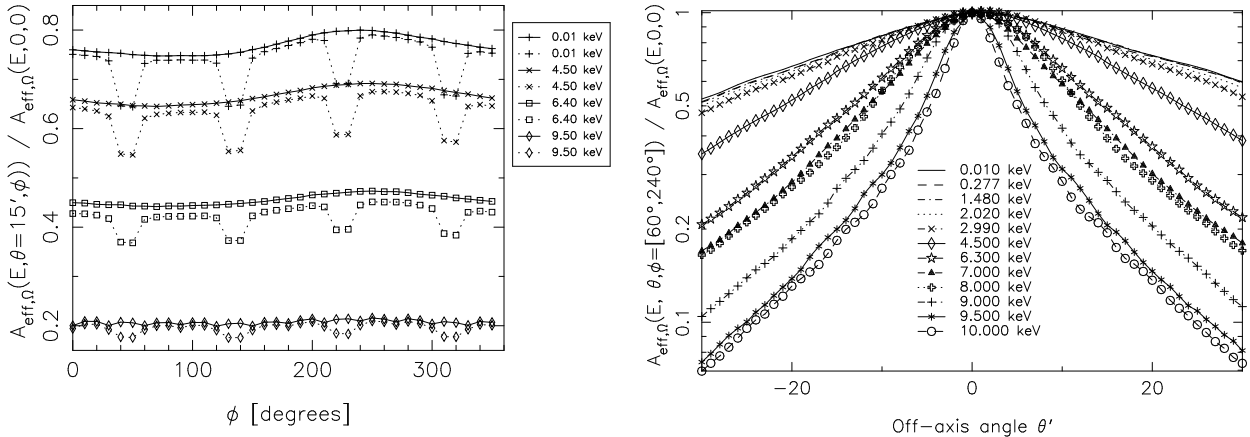
Figure 18: Left: Energy-dependent vignetting as a function of angle for a number of energies. This is a slice taken approximately through the axis of greatest asymmetry. Right: Energy-dependent vignetting for $\theta = 15'$ as a function of $\phi$ for 4 energies. The top curve for each energy shows $A_{eff,\Omega=2\pi}(E,\theta,\phi)/A_{eff,\Omega=2\pi}(E,0,0)$, while the lower curves show the effect of clipping by a square corresponding to the HRC-I clear aperture; see Gaetz et al. (2000).

loop. Fig. 19 compares a ground-calibration image to a raytrace simulation, indicating features of interest. The HRMA was designed to suppress single-reflection ghost images from reaching within a radius of $14'$ of the optical axis.

At off-axis angles of $\theta \sim 25'$, the single-reflect P and H ghosts for mirror pair 6 cross through the direct image. (The mirror pair 3 and 4 ghosts cross over at $\sim 35' - 40'$.) As the ghost forms a cusp, the surface brightness is enhanced which may make the ghost more noticeable.

## 8.1   Analysis Issues

- Faint arc-like structures $> 14'$ off-axis may be single-reflection ghost images. Bright sources can produce ghosts which fall on the detector even if the direct image of the source misses the detector. Because the ACIS-S and HRC-S detectors reach larger off-axis angles, single-reflection ghosts are more likely to be seen there.

# 9   Summary of PSF Features

- The PSF is energy dependent, particularly above $\sim$4–5 keV as the larger mirror pairs successively drop out.

- The mirror pair focal planes are curved toward the mirrors; the focal planes for the smaller mirrors are more strongly curved than those for the the larger mirrors. This results in an energy-dependence for the mean HRMA focal plane. Because the detectors do not fully follow the focal plane curvature, off-axis images are somewhat out of focus, the degree of which is energy-dependent. (§1.2; Figs. 2, 4.)

- The on-axis PSF "puffs out" with increasing energy. At the highest energies, the PSF core is extended (scale $\sim$0.6$''$) because of a "tilt ring" due to a misalignment in the smallest mirror pair (§2; Fig. 7).
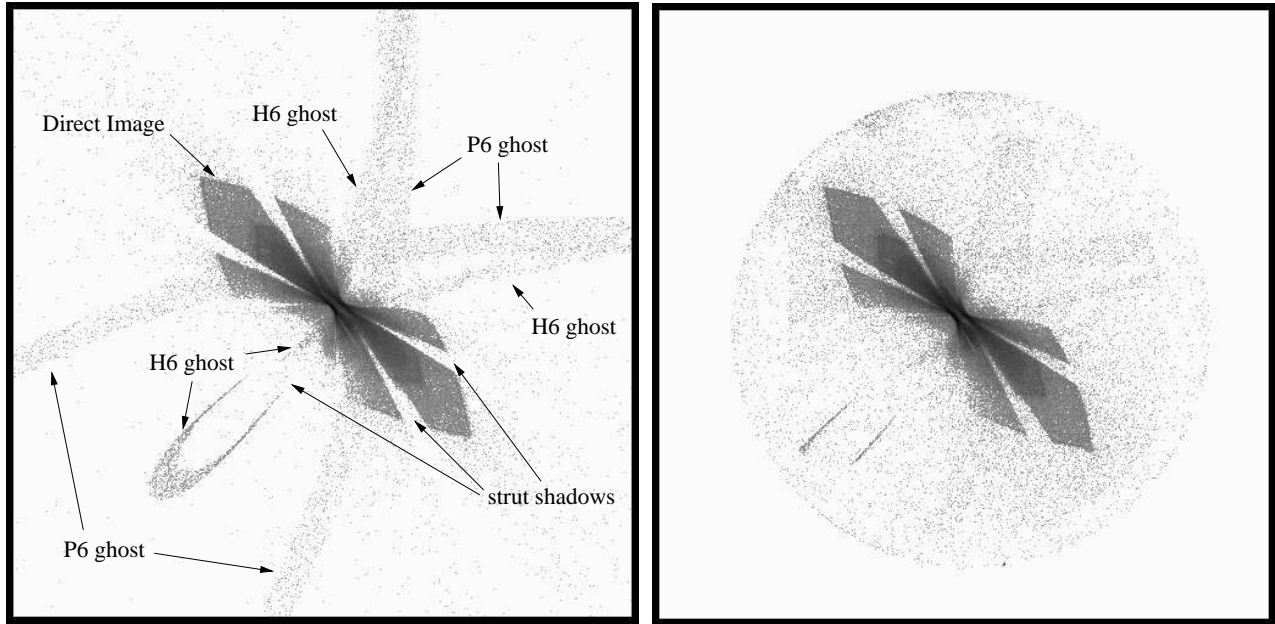
Figure 19: Left: SAOsac simulation of single-reflection ghosts for a monochromatic 0.277 keV source 30 ′ off-axis. This simulation may be compared directly to the corresponding ground calibration. The largest bow-tie shape for the direct image results from mirror pair 6, the smallest mirror pair; the image from mirror pair 4 is also seen as an overlapping bow tie about $\frac{2}{3}$ the size of the large one. Mirror pairs 3 and 1 also contribute with even smaller overlapping bow ties. Right: Ground calibration image corresponding to the simulation. The disk shows the full extent of the detector surface, but portions are masked off by a detector mask. In particular, the ghost loop in the lower left is obstructed by a mask in the detector. The outline of the detector mask can be seen faintly by the enhanced density of counts; note for example where the ghost images cut off in the upper right.

- Faint mirror scattering wings extend to large distances, falling very roughly as $\theta^{-2}$ where $\theta$ is the angle from the direct (specular) image. The scattering wings are energy dependent. The spectrum of the scattered wings varies with distance from the source, becoming harder radially outwards. (§5; Figs. 12–17.)

- The off-axis PSF expands very roughly (but more slowly than) quadratically with off-axis angle. (§3; Fig. 6.)

- Because of misalignments, the PSF exhibits bright substructure (and overall deformations) varying as $\phi/2$, rather than as $\phi$ which would be expected for the case of azimuthal symmetry. (§3; Fig. 4.)

- Bright PSF substructure can be mistaken for multiple close sources, particularly for poorly sampled sources; even for brighter sources, detect algorithms may be fooled into seeing multiple close sources. (§4; Fig. 11.)

- Vignetting is strongly energy dependent at higher energies (above $\sim$4–5 keV).

- Support struts in the optical path produce shadows at the focal plane; these can show up in sufficiently well sampled images. On-axis, they manifest as twelve evenly spaced narrow spokes (Fig. 13). Off-axis, the spokes may show lateral offsets (Figs. 4, 10).
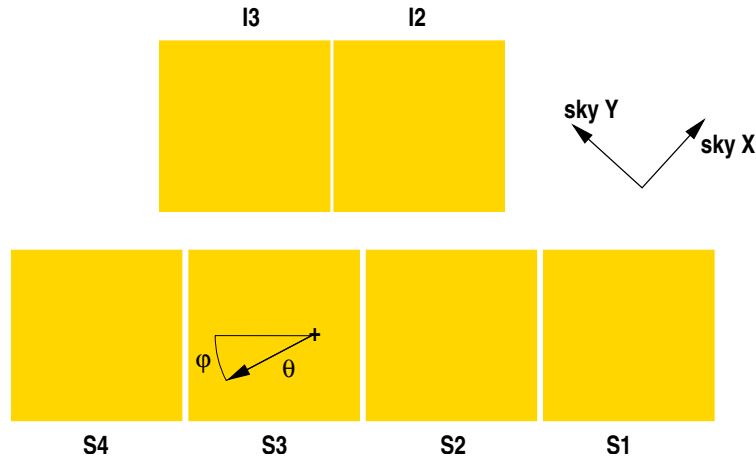
Figure 20: Schematic of $\theta$ and $\phi$ conventions (ACIS-S aimpoint). Note that $\theta$ and $\phi$ are defined in a frame fixed to a telescope coordinate frame (MSC coordinates), and not to the sky coordinate system. The tool `dmcoords` (CXC:CIAO) can be used to derive `THETA` and `PHI` for a given observed source.

- Bright sources far off-axis can produce faint single-reflection ghosts. The design of the optics suppresses these within $\sim 14'$ of the optical axis. (§8; Fig. 19.)

## 10    Coordinate Systems

The conventions for $\theta$ and $\phi$ (Mirror Spherical Coordinates, or MSC) are illustrated in Fig. 20. This is a system tied to the telescope frame; the tool `dmcoords` (CXC:CIAO) can be used to determine these coordinates (`THETA` and `PHI`) for a given position on the detector. A fuller discussion of *Chandra* coordinate systems is given in McDowell (2001).

## 11    Simulations of HRMA Performance

Many of the imaging characteristics are illustrated with simulations of the HRMA using SAOsac (Jerius et al., 1995) and the `orbit_XRCF+tilts_04` configuration (Jerius, 2001). These simulations incorporate our best current understanding of the HRMA performance; the SAOsac model underlies the CXC web based PSF tool `ChaRT` (http://cxc.harvard.edu/chart/; see also the caveats page http://cxc.harvard.edu/chart/caveats.html). The raytrace model currently underpredicts mirror scattering.

## References

Aldcroft, T. 2002: Image reconstruction performance, http://cxc.harvard.edu/cal/ASPECT/ img_recon/report.html

Boese, F. G. 2000: Astron. Ap. Suppl. **141**, 507

CXC:CIAO, http://cxc.harvard.edu/ciao/

Gaetz, T. 2004a: Analysis of the Chandra On-Orbit PSF Wings, `http://cxc.harvard.edu/cal/Hrma/psf/wing_analysis.ps`

Gaetz, T. 2004b: Assessing the Chandra PSF Wings: An Estimate from Ground Calibration Data, `http://cxc.harvard.edu/cal/Hrma/psf/XRCF_PSF_wing_profile`

Gaetz, T. J., Jerius, D., Edgar, R. J., Van Speybroeck, L. P., Schwartz, D. A., Markevitch, M. L., Taylor, S. C., and Schulz, N. S. 2000: in Proc. SPIE Vol. 4012, p. 41-52, X-Ray Optics, Instruments, and Missions III, Joachim E. Truemper; Bernd Aschenbach; Eds., pp 41–52

Jerius, D. 2001: `http://hea-www.harvard.edu/MST/simul/raytrace/databases/ts_config/orbit_XRCF+tilts_04.html`

Jerius, D. 2002: Comparison of on-axis Chandra Observations of AR Lac to SAOsac Simulations, `http://cxc.harvard.edu/cal/Hrma/psf/ARLac-onaxis.ps`

Jerius, D., Freeman, M., Gaetz, T., Hughes, J. P., and Podgorski, W. 1995: in ASP Conf. Ser. 77: Astronomical Data Analysis Software and Systems IV, Vol. 4, pp 357–+, `http://adass.org/adass/proceedings/adass94/jeriusd.html`

Juda, M. 2002: Blur from Residual Errors in HRC Event Position Reconstruction, `http://hea-www.harvard.edu/~juda/memos/hrc_blur/hrc_blur.html`

Kim, D.-W., Cameron, R. A., Drake, J. J., Evans, N. R., Freeman, P., Gaetz, T. J., Ghosh, H., Green, P. J., Harnden, F. R., Karovska, M., Kashyap, V., Maksym, P. W., Ratzlaff, P. W., Schlegel, E. M., Silverman, J. D., Tananbaum, H. D., Vikhlinin, A. A., Wilkes, B. J., and Grimes, J. P. 2004: Astrophys. J. Suppl. **150**, 19

McDowell, J. 2001: Coordinate Systems for Analysis of On-Orbit Chandra Data. Paper I: Imaging, `http://asc.harvard.edu/contrib/jcm/ncoords.ps`